

Research Article

Test on Hysteretic Behaviour of Prestressed Composite Joints with Concrete-Encased CFST Columns

Kun Wang ^{1,2} and Huihui Luo³

¹College of Civil Science and Engineering, Yangzhou University, Yangzhou 225127, China

²Jiangsu Hanjian Group Company Limited, Yangzhou 225000, China

³College of Guangling, Yangzhou University, Yangzhou 225127, China

Correspondence should be addressed to Kun Wang; wangkun@yzu.edu.cn

Received 11 June 2019; Revised 25 July 2019; Accepted 28 July 2019; Published 14 August 2019

Academic Editor: Rosario Montuori

Copyright © 2019 Kun Wang and Huihui Luo. This is an open access article distributed under the Creative Commons Attribution License, which permits unrestricted use, distribution, and reproduction in any medium, provided the original work is properly cited.

Four composite joint specimens consisted of concrete-encased steel beams and concrete-encased concrete-filled steel tube (CFST) columns were tested under lateral cyclic loading, in which three specimens were prestressed and the other was not. In the tests, crack distributions and failure modes of the joint specimens were acquired, and the energy dissipation, rigidity degeneration, ductility, and residual deformation were investigated. Meanwhile, the strain variation of longitudinal rebars and I-steel flanges at beam ends as well as steel tubes in panel zones were analysed. The experimental results showed that a type of mixed mode consisting of shear failure in the panel zone and flexural failure at beam ends was found for three prestressed joint specimens, whilst only flexural failure at beam ends was observed for the non-prestressed one, and all joint specimens showed good hysteretic behaviour. In addition, as can be seen from the skeleton curves, the lateral peak loads of prestressed joint specimens could be enhanced to some extent by increasing the prestressing level, and the axial compression ratio had little effect on lateral loads; meanwhile, the ductility and energy dissipation for prestressed joint specimens also could be reduced by increasing the prestressing level and axial compression ratio.

1. Introduction

Prestressed concrete-encased steel frames combined the advantages of concrete-encased steel frames and prestressed reinforced concrete frames, such as higher sectional bearing capacities, preferable ductility, better energy dissipation, and smaller deflection and crack widths; thus, they have been extensively studied and utilized in China in recent years [1–5].

In general, H-steels or I-steels are used in beams, and two crossed H-steels are welded together in columns for prestressed concrete-encased steel frames. However, engineering practices indicate that the prestressing tendons in beams are likely to run through the flanges of H-steels in the panel zones, which results in complex connection details; in addition, the shear capacities in panel zones could be decreased by the prestressing ducts. Therefore, an innovative

prestressed composite frame was proposed, as shown in Figure 1, in which the conventional composite columns were replaced by concrete-encased concrete filled steel tube (CFST) columns [6]. In previous work, two composite frame specimens with concrete-encased CFST columns were tested and analysed, and the results showed that the innovative prestressed composite frames showed good seismic performance [7].

Concrete-encased CFST columns are innovative components based on CFST columns. At present, amounts of test and numerical analysis on CFST members have been reported [8–12], which showed high bearing capacity, high stiffness, and good seismic performance. When compared with CFST columns, concrete-encased CFST columns can not only avoid complicated treatment for corrosion and fire prevention but also have the advantage for the steel tube to pass through the frame joints easily. Han and An [13]

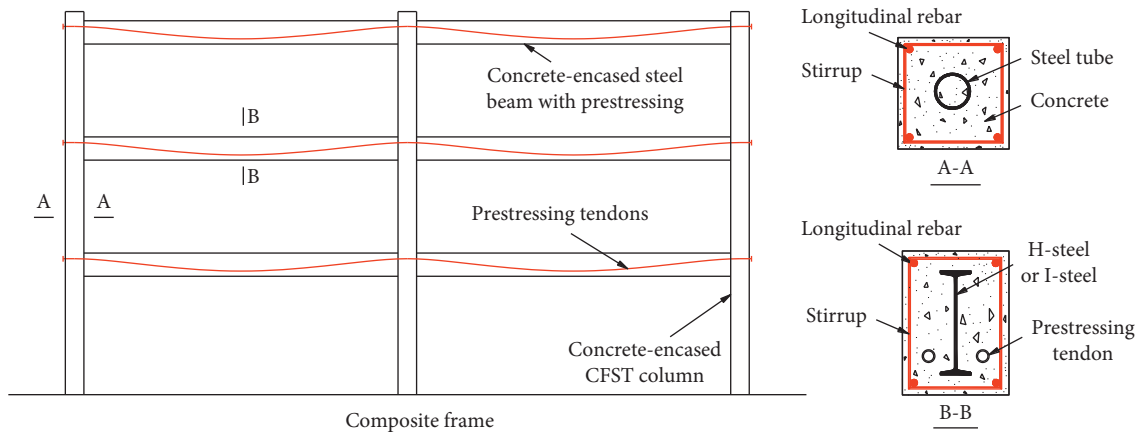


FIGURE 1: Sketch of the innovative prestressed composite frame.

studied the performance of concrete-encased CFST columns under axial compression by tests, and three types of simplified ultimate strength formulae were built. An and Han [14] and Guo et al. [15] conducted tests on concrete-encased CFST columns under combined compression and bending, and the cross-sectional bending capacity formulae were proposed, respectively. Han et al. [16] tested nine concrete-encased CFST columns under constant axial load and cyclically increasing flexural loading and pointed out that the columns exhibited good energy dissipation and ductility. Qian et al. [17] built a hysteretic model of moment-curvature curves for concrete-encased CFST columns subject to lateral loading by tests and finite element analysis. In addition, Ji et al. [18, 19] tested the hysteretic behaviour and cumulative seismic damage of concrete-encased CFST columns, and the strength capacity design formulae were developed by the superposition method.

For composite beams, Liu et al. [20] studied the flexural strength of simply supported steel-concrete composite beams by tests and numerical analysis; Wang et al. [21] proposed bending capacity formulae for the prestressed concrete-encased steel beams according to the tests; Huang et al. [22] investigated the behaviour of prestressed CFST truss girders and found out that flexural strength and the failure modes of the girders were influenced by prestressing levels and shear span-to-depth ratios; Kim et al. [23, 24] tested the flexural performance of prestressed composite beams with corrugated web and introduced a flexural behaviour mechanical model; otherwise, Choy et al. [25], Yao et al. [26], and Wang et al. [27] tested the shear performance of prestressed concrete-encased steel beams, respectively, and the contributions of concrete and embedded H-steels were fully discussed.

For composite joints, Li et al. [28] tested the seismic performance of two kinds of CFST column-RC beam joints that are connected by vertical or U-shaped steel plates and studs and bending capacity of joints increased compared to the RC joints; Qian and Jiang [29] tested the joints consisting of reinforced concrete beams and concrete-encased CFST columns under cyclic loading, and it is observed that the energy dissipation capacity could be enhanced and the shear deformation could be decreased when the stirrup spacing

reduced in the panel zones for weak joints; Liao et al. [30] and Nie et al. [31] pointed out that the composite joints consisting of reinforced concrete beams and concrete-encased CFST columns with the outer stiffening ring also showed good hysteretic behaviour; Qian et al. [32] investigated the mechanical mechanism of composite joints consisting of steel beams and concrete-encased CFST columns by validated numerical model, and it is found that the positive and negative capacities of the spatial joints under bidirectional loading were about 14% and 18% lower than those of the planar joints; additionally, Deng et al. [33] experimentally studied the crack development and rigidity of joints consisting of prestressed reinforced concrete beams and concrete-encased CFST columns. Although a number of tests and analysis on composite joints with concrete-encased CFST columns have been performed, so far seismic performance and design approaches for the proposed innovative prestressed composite joints have not been reported.

Therefore, in order to study the seismic behaviour of the proposed prestressed composite joints, three prestressed interior joint specimens and a non-prestressed one were made and tested under lateral cyclic loading. During the tests, the crack development and failure modes were observed, and rigidity degeneration, deformation restoring capacity, ductility, energy dissipation, shear deformation, and strain variations were analysed. The testing results could provide a basis for promoting the application of such frame structures in seismic zones.

2. Experimental Programs

2.1. Test Specimens. In recent research, Montuori et al. [34, 35] found that slab, joist, and desk have important effect on lateral stiffness under gravity and horizontal loads for RC buildings, and the equivalent beam approach was proposed for calculation. However, in order to simplify the joint design scheme in the tests, the foregoing effects were not considered. The inflection points of beams and columns in a frame are assumed to occur at the midpoint when subjected to lateral loads [36], and four composite frame interior joint specimens with concrete-encased CFST columns were

designed and denoted as S-1 to S-4, in which the specimens S-1~S-3 were prestressed and S-4 was not. The configuration of four joint specimens is shown in Figure 2. All specimens had the same cross section with the size of 300 mm × 350 mm for beams and 350 mm × 350 mm for columns. In addition, I-steels of 22a with a size of 220 mm × 110 mm × 7.5 mm × 12.3 mm and circular steel tubes of 108 mm × 8 mm were arranged inside the beams and columns, respectively; two inner diaphragms with the thickness of 11 mm were used to strengthen the connection of I-steels and steel tube in the panel zone for each specimen according to the Chinese Specification JGJ3-2010 [37].

In the actual practice, the prestressing tendons were applied in the form of three-segment parabola in beams, which run through the joint from the upper sides at beam ends. For the convenience of specimen making and later analysis, the prestressing tendons were arranged in straight lines with the bond posttensioned technique, which pass through the joint from the two sides of steel tubes. The prestressing tendons with nominal diameters of 12.7 mm and 15.2 mm were adopted in the beams, and the ducts were grouted after tension. During the tensioning, the strains of the tendons were measured by calibrated self-made force transducers. The measured effective prestress of tendons for specimens S-1, S-2, and S-3 was 1268 MPa, 1214 MPa, and 1221 MPa, respectively.

All joint specimens were designed in accordance with the criterions of “strong column weak beam” and “strong shear weak bending,” and the major parameters involving axial compression ratio (n_0) and prestressing level (λ) are listed in Table 1.

According to [18], the axial compression ratio (n_0) is given as follows:

$$n_0 = \frac{N}{f_{co}A_{co} + 0.9f_{ci}A_{ci}(1 + 1.8\xi)}, \quad (1)$$

where N is the vertical load applied on top of columns; f_{co} and f_{ci} are the axial compressive strength of concrete in the outer and inner steel tube, respectively; A_{co} and A_{ci} are the cross-sectional area of concrete in the outer and inner steel tube, respectively; and ξ is the confinement index of the CFST core.

Neglecting the contribution of I-steel web, the prestressing level (λ) could be calculated by using the following equation:

$$\lambda = \frac{A_p f_{py} h_p}{A_p f_{py} h_p + A_{ss} f_{ss} h_{ss} + A_s f_y h_s}, \quad (2)$$

where A_p , A_{ss} , and A_s are the cross-sectional area for tendons, tensile flange of I-steel, and tensile longitudinal rebars in beam, respectively; f_{py} , f_{ss} , and f_y are the tensile yielding strength for tendons, I-steel, and tensile longitudinal rebars; and h_p , h_{ss} , and h_s are the distance from centroid of tendons, tensile flange of I-steel, and tensile longitudinal rebars to extreme compressive fibre, respectively.

The other related design parameters, such as vertical load (N) on top of columns, amount of tendons, and the summations of moments ($\sum M_b$ and $\sum M_c$) at beams and columns ends, are also listed in Table 1.

2.2. Material Properties. All specimens were poured and cured by the same batch of concrete with a strength grade of C40, and several concrete test cubes of 100 mm × 100 mm × 100 mm were reserved to obtain the compressive strength in the same conditions. By mean of the material mechanical property tests, the average concrete cubic compressive strength (f_{cu}) is 46.1 MPa, and the average axial compressive strength (f_c) and elastic modulus (E_c) are calculated as 35.0 MPa and 3.39×10^4 MPa based on GB/T 50152-2012 [38], respectively.

In the specimens, the grade of I-steels, steel diaphragms, and steel tubes is Q235, and the grade of longitudinal rebars and stirrups is HRB400. The mechanical properties of steels by tests are given in Table 2.

2.3. Testing Setup and Measurements. In order to simulate the hysteretic behaviour of frame joints well under earthquake action, displacement loading at top of the upper column was adopted by an MTS actuator in the tests, and a general view of test setup was illustrated in Figure 3. In the test setup, two sliding bearings were used to support the beam cantilevered ends far from columns, in which only lateral movement and rotation were permitted, and a fixed hinge bearing was used to support the bottom of the lower column. Additionally, a self-balancing apparatus was used to impose the vertical load on the top of the upper column, which consisted of a hydraulic jack, four high-strength steel rods, and two welded rigid steel plates. The horizontal length between the centres of two sliding bearings was 3550 mm, and the vertical distance from lateral loading point to the fixed hinge bearing centre was 1750 mm.

During the loading, the vertical load (N) was firstly imposed to 30% of the predetermined value and then unloaded to zero; after that, the vertical load reached the predetermined value again and was kept constant. The lateral load (P) by displacement control was applied at the top of column according to ANSI/AISC 341-05 [39], and the loading history was listed in Table 3, where the lateral displacements were calculated by interstory drift ratios. When the lateral load dropped to 85% of the peak load or the lateral displacement reached a large value which was not suitable for loading, the lateral loading aborted.

2.4. Measurements. In order to study strain variations and obtain the mechanical mechanism of specimens, strain gauges were fixed on I-steel flanges, longitudinal rebars at beam and column ends and on stirrups in panel zones, and five strain rosettes were mounted on steel tubes in panel zones. The measuring point arrangement was given in Figure 4. Additionally, two intersecting potentiometers were fixed in the panel zone to obtain the shear deformation.

The main measurements include (1) the load-displacement (P - Δ) curves subjected to lateral cyclic loading, (2) the crack distribution and the failure modes, (3) the strain variations of I-steel flanges, longitudinal rebars, stirrups, and steel tubes, and (4) shear deformation of panel zones.

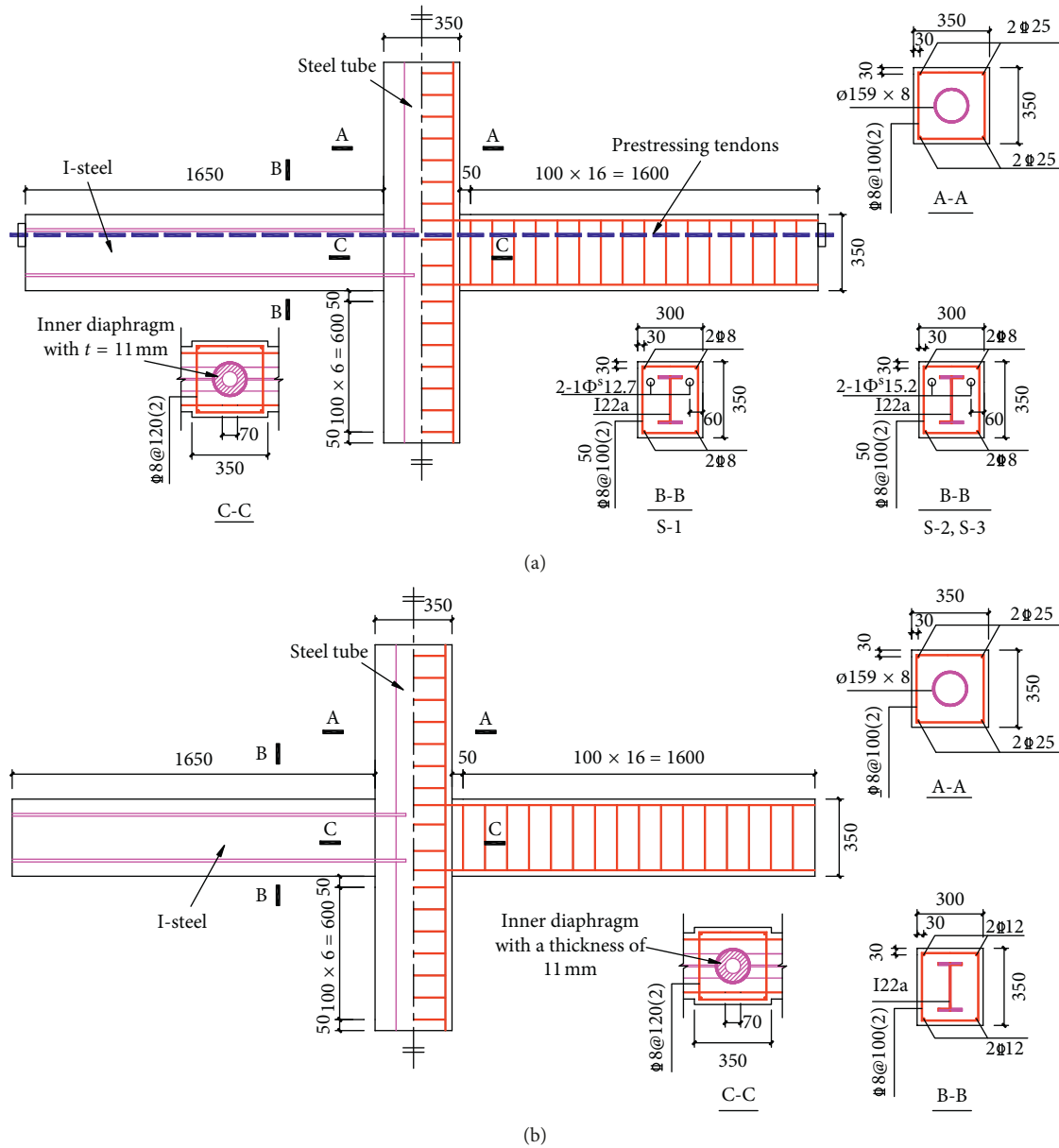


FIGURE 2: Reinforcements of specimens (units: mm): (a) S-1, S-2, and S-3; (b) S-4.

TABLE 1: Design parameters of specimens.

Specimens	Axial compressive ratio n_0	Vertical load (N/kN)	Prestressing level (λ)	$\sum M_b$ (kN·mm)	$\sum M_c$ (kN·mm)	$\sum M_c / \sum M_b$
S-1	0.29	1630	0.39	372	627	1.69
S-2	0.14	815	0.50	395	600	1.52
S-3	0.29	1630	0.50	395	627	1.59
S-4	0.29	1630	—	343	627	1.83

3. Testing Procedures

3.1. *Experimental Observations.* The testing of specimens under lateral cyclic loading was well performed. For the convenience of describing the experimental observation, forward loading was appointed as the right direction. The whole loading process could be described as follows:

- (1) The observation of specimens S-1 and S-3 was almost analogous. When the displacement reached ± 6.6 mm, several vertical flexural cracks with a width of about 0.03 mm and length of about 150 mm were found on the lower sides at two beam ends which were closed to columns, and no cracks were found on the upper sides; after that, new flexural cracks

TABLE 2: Mechanical properties of steels.

Components	Size	Yielding strength	Tensile strength
		f_y (MPa)	f_u (MPa)
I-steels	I22a	288.1	499.0
Steel diaphragms	-12	291.2	488.3
Steel tube	$\phi 159 \times 8$	255.0	425.0
	$\phi 8$	388.4	562.2
Steel bars	$\phi 12$	402.3	570.6
	$\phi 25$	445.3	613.7
Tendons	$\phi^s 12.7$	1494	1717
	$\phi^s 15.2$	1679	1930

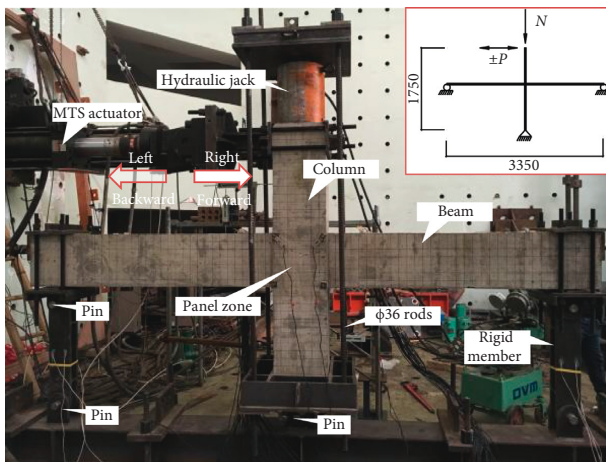


FIGURE 3: A general view of the test setup (units: mm).

TABLE 3: Loading history for test specimens.

Displacements (mm)	Interstory drift ratios (%)	Numbers of loading cycles
± 6.6	± 0.375	6
± 8.8	± 0.5	6
± 13.1	± 0.75	6
± 17.5	± 1.0	4
± 26.3	± 1.5	2
± 35	± 2.0	2
± 52.5	± 3.0	2
± 70	± 4.0	2
± 87.5	± 5.0	2

occurred on beams and existing cracks propagated. When the displacement increased to ± 13.1 mm, two crossing inclined cracks with a width of about 0.1 mm formed in the panel zone, and some new vertical cracks appeared on the upper sides of beams. With the lateral displacement increased to ± 26.3 mm, the concrete was slightly crushed on top and bottom of beam ends, and some new short inclined cracks appeared in the panel zone. As the lateral displacement increased to ± 52.5 mm, the concrete in the panel zone peeled off and several crossing cracks propagated to columns, whilst the lateral load reached the peak value and the crushing concrete at beam ends got worse. Since then, the

damage of concrete in the panel zone enhanced due to the increase of shear deformation. When the lateral displacement reached ± 105 mm, the damage of concrete in the panel zone was very serious, and the lateral load dropped to 85% of the peak value.

- (2) For specimen S-2, when the lateral displacement was ± 6.6 mm, several vertical flexural cracks occurred on lower sides at beam ends, and two crossing cracks were found in the panel zone at the displacement of ± 8.8 mm subsequently. When the displacement reached ± 13.1 mm, some flexural cracks were found on the upper sides at beam ends. With the increase of lateral displacements, the concrete at two beam ends was slightly crushed at the displacement of ± 26.3 mm, and the concrete in the panel zone began to spall at the displacement of ± 35.0 mm. When the lateral displacement increased to ± 52.5 mm, the damage of concrete in the panel zone was aggravated, and the concrete at beam ends began to peel off. When the displacement reached ± 105 mm, the concrete in the panel zone spalled seriously and the specimen S-2 failed.
- (3) The representation of specimen S-4 was distinct from that of prestressed ones. When the lateral displacement was ± 6.6 mm, vertical flexural cracks were found on both of upper and lower sides at beam ends simultaneously, and as the displacement increased to ± 8.8 mm, the crossing cracks formed in the panel zone. When the lateral displacement reached ± 26.3 mm, slightly concrete crushing was observed at beam ends. With the increase of lateral displacement, the concrete crushing at beam ends was aggravated and some vertical flexural cracks run through the beam sections. Additionally, several new crossing cracks occurred in the panel zone. Finally, the specimen S-4 failed at the displacement of ± 87.5 mm in the second displacement cycle, and no concrete crushing in panel zone was found.

3.2. Crack Distributions and Failure Modes. The final crack distributions of all specimens are illustrated in Figure 5, which include flexural cracks at beam ends and crossing cracks in panel zones. With the increase of displacements, it is observed that the vertical flexural cracks first appeared at beam ends and propagated to the beam axis showing a trend of penetration and then crossing cracks appeared in the panel zone. Due to the prestressing effect, the cracks at beam ends were postponed to occur until the displacement increased to ± 13.1 mm for specimens S-1~S-3, and these cracks were asymmetric relative to the beam axis; for specimen S-4 without prestressing, cracks first occurred at the displacement of ± 6.6 mm at beam ends, and cracks on beam developed symmetrically. After yielding for all specimens, cracks on the beams far from columns stopped propagating, and the concrete at beam ends was crushed to peel off gradually. In addition, a few slight horizontal and inclined cracks were observed on two columns.

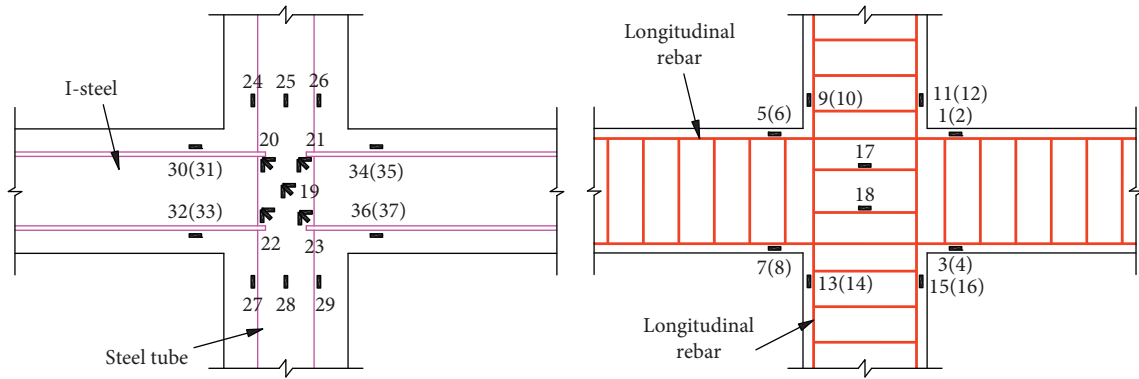


FIGURE 4: Arrangements of measuring points.

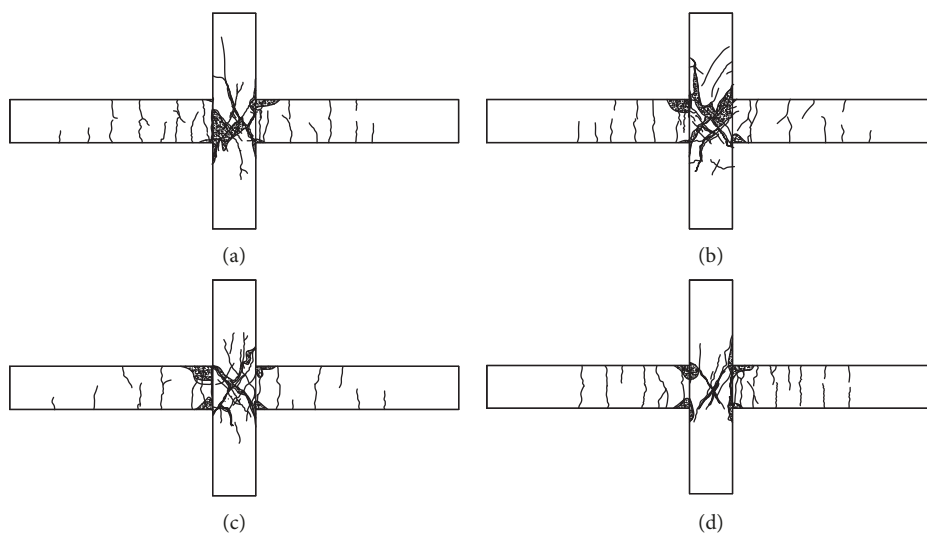


FIGURE 5: Crack distributions for joint specimens: (a) S-1; (b) S-2; (c) S-3; (d) S-4.

Under the cyclic loading, the concrete on upper and lower sides of two beam ends was slightly crushed when the lateral displacement reached ± 26.3 mm, which signified that the flexural bearing capacities for beams were reached, whilst no evident concrete crushing was found in the panel zones at this time. Since the concrete-encased steel beams showed good ductility and basically kept the flexural bearing capacities after concrete crushing, the shear deformation and crossing crack widths in panel zones continued to increase with the increasing rotation of plastic hinges at beam ends. When lateral loads reached peak values, shear failure in panel zones with concrete crushing was observed for specimens S-1, S-2, and S-3. However, due to the comparatively lower bending capacity of beams, only flexural failure at beam ends was acquired for specimen S-4. The failure modes of all specimens are illustrated in Figure 6.

As can be seen from the loading process, the failure mode for specimens S-1, S-2, and S-3 was a mixed pattern, which consisted of initial flexural failure at beam ends and subsequent shear failure in the panel zone; whilst only flexural failure was found at beam ends for specimen S-4. The reason for mixed failure was that the bending moment at

beam ends was almost unchanged, and the distance between the points of sectional tensile and compressive resultant forces reduced by concrete crushing at beam ends; thus, the resultant forces enhanced, which were transmitted into joints and led to an increase of shear forces in panel zones.

4. Test Results and Analysis

4.1. Lateral Load-Displacement Hysteretic and Skeleton Curves. Figure 7 shows the lateral load-displacement hysteretic curves for all specimens. As can be seen, the hysteretic curves followed a straight line in the initial phase, which means that the specimens were in the elastic stage. After yielding, the areas of the hysteretic loops increased gradually showing spindle shapes, and some residual deformation were observed after unloading; after the peak value, the lateral loads decreased slowly with the increase of lateral displacements, which showed good ductility. In an overall view, since the hysteretic curves were plump without obvious pinching, all joint specimens presented good seismic performance.

Skeleton curves could be used to reflect the characteristics of lateral loads and ductility, which are significant for

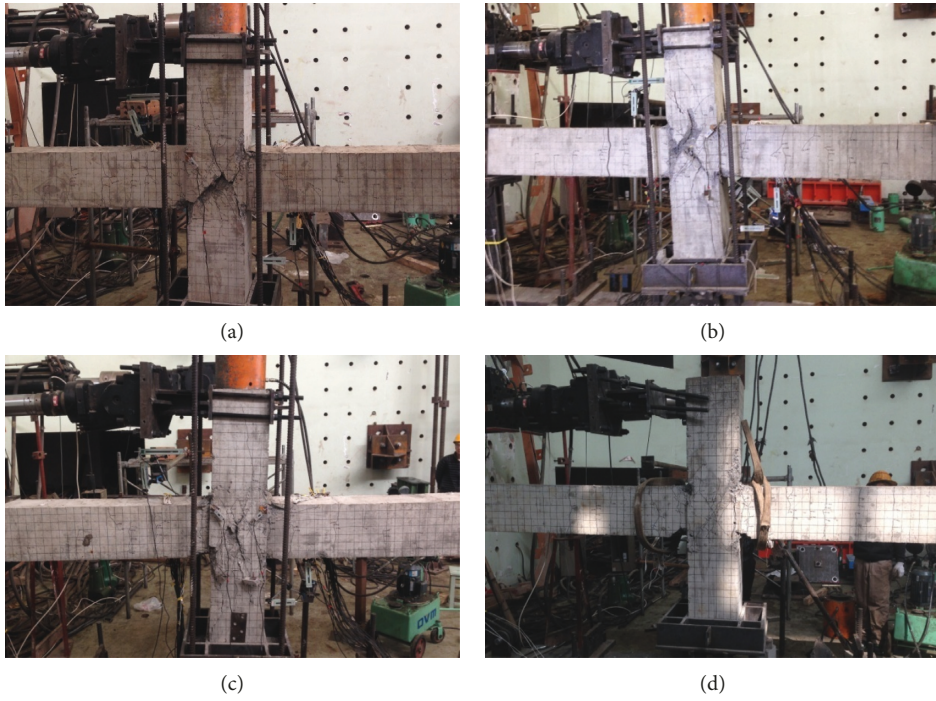


FIGURE 6: Failure modes for joint specimens: (a) S-1; (b) S-2; (c) S-3; (d) S-4.

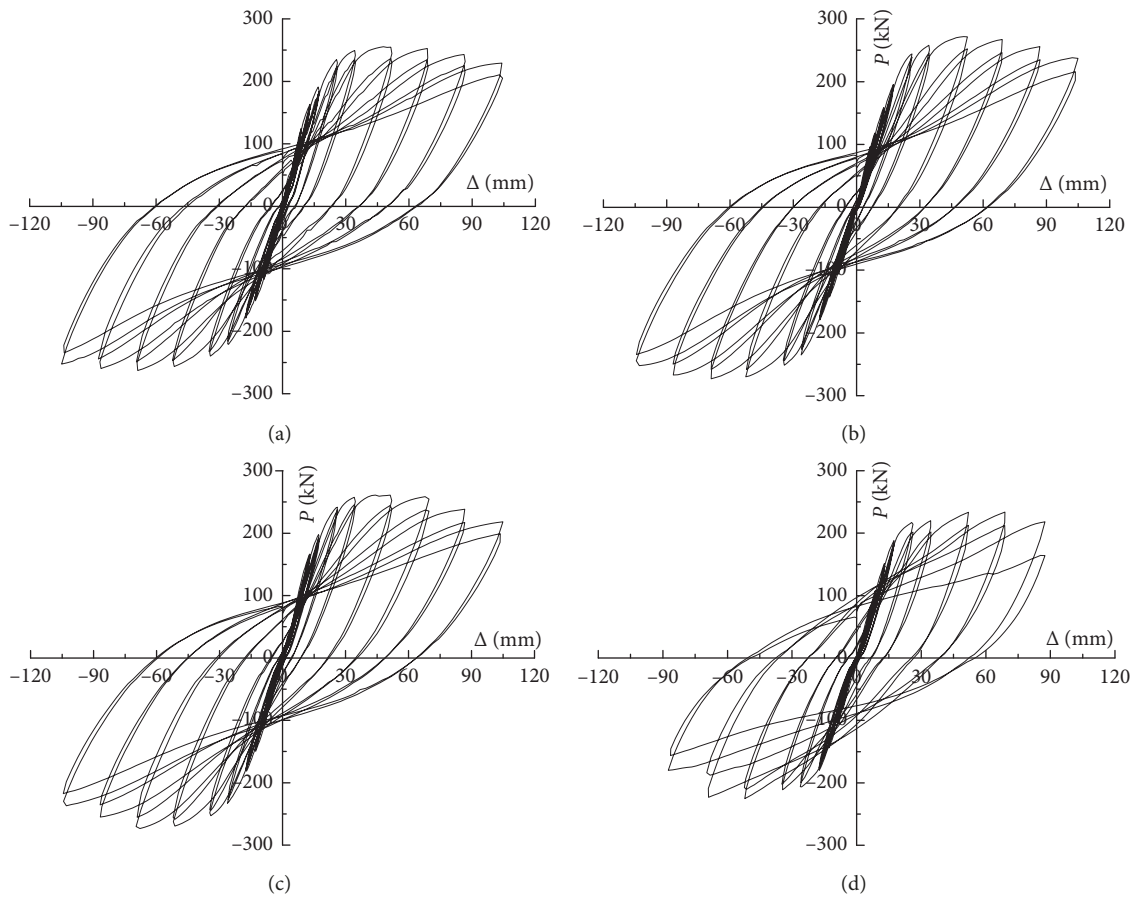


FIGURE 7: Hysteretic curves of joint specimens: (a) S-1; (b) S-2; (c) S-3; (d) S-4.

determining the hysteretic models. Figure 8 gives the skeleton curves of all joint specimens. It shows that the lateral loads slightly improved and ductility decreased when the prestressing level increased from 0.39 to 0.50 by contrasting specimen S-1 with S-3. With an increase in axial compression ratio from 0.14 to 0.29 for specimens S-2 and S-3, the lateral loads were almost the same, but the ductility reduced to a certain degree. It should be noted that the lateral peak load of specimen S-4 was the lowest, and the reason for this was that only bending failure occurred at two beam ends. In addition, the descending branches of skeleton curves for all specimens were more gradual, which showed preferable ductility.

4.2. Energy Dissipation. Energy dissipation capacity is one of the most important indices to estimate the seismic behaviour of joint specimens. The relation between energy dissipation coefficient (E_d) and lateral displacement (Δ) is shown in Figure 9. Due to the fact that the plastic hinges at two beam ends developed fully, the energy dissipation capacity for specimen S-4 was evidently higher than the others after yielding. However, the energy dissipation coefficients for specimens S-1 and S-3 with different prestressing levels were quite close to each other, which means that the prestressing level had a limited effect on energy dissipation. As the axial compression ratio increased from 0.14 to 0.29 for specimens S-2 and S-3 subject to the same prestressing level, the energy dissipation capacities of specimens enhanced significantly.

4.3. Rigidity Degradation. Figure 10 gives the loop rigidity coefficient (K) versus lateral displacement (Δ) curves for all specimens in forward and backward directions. It was observed that the loop rigidity coefficients reduced as the lateral displacement increased, and the rigidity degradation curves of prestressed joint specimens were quite close; however, the loop rigidity coefficients of specimen S-4 were lower than that of prestressed ones at each cycle after yielding, which was due to the distinct failure modes.

4.4. Deformation Restoring Capacity. Figure 11 shows the relationship of residual deformation ratios (Δ_0/Δ_m) and lateral displacements (Δ) for all specimens, where Δ_m is the experienced maximum lateral displacement at each cycle and Δ_0 is the corresponding residual deformation after unloading. It is found that the residual deformation ratios of specimen S-4 were greater than the others at each cycle after yielding in two directions, which was due to the fact that larger residual deformation generated by sufficiently developed plastic hinges at beam ends.

In addition, it was observed that the residual deformation ratios of specimen S-3 were smaller than that of S-1, and the ratios of specimen S-2 were lower than that of S-3 after the elastic stage in forward loading, which means that the residual deformation could decrease by increasing the prestressing levels or by reducing the axial compressive ratios, respectively. In the reversed direction, the values of residual deformation ratios for specimens S-1, S-2, and S-3

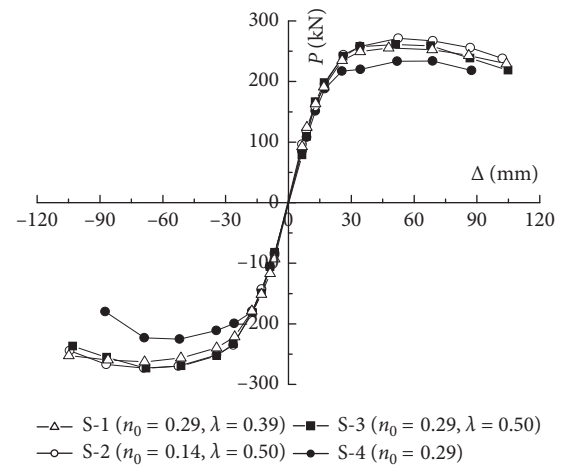


FIGURE 8: Skeleton curves of joint specimens.

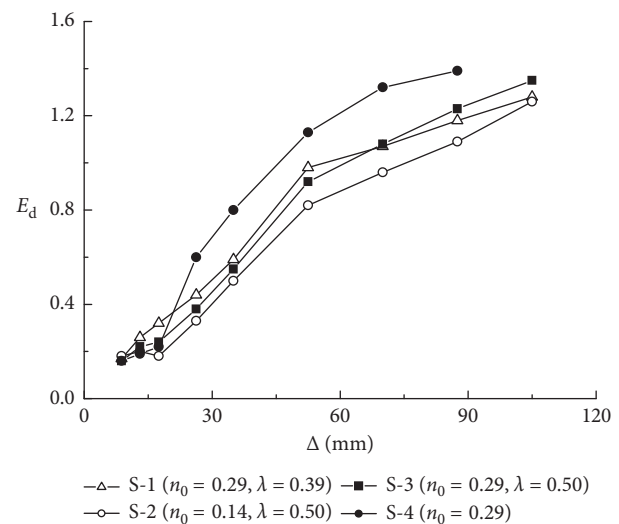


FIGURE 9: Energy dissipation coefficient (E_d) vs. displacement Δ .

were almost equal, and this could be attributed to the Bauschinger effect of the embedded I-steels and steel tubes.

4.5. Ductility. Displacement ductility factor ($\mu = \Delta_u/\Delta_y$) could be used to evaluate the ductility performance for joint specimens, where Δ_y is the yielding displacement in skeleton curves and Δ_u is the ultimate displacement corresponding to the lateral load dropped to 85% of the peak value. In this paper, the yielding points for skeleton curves were calculated by the general yield moment method [40].

Table 4 listed the yielding loads (P_y) and corresponding displacements (Δ_y), the peak loads (P_u), the ultimate displacements (Δ_u), displacement ductility coefficients (μ), and mean displacement ductility factors ($\bar{\mu}$) in forward and backward loading for all specimens. It can be seen that displacement ductility coefficients in forward were slightly higher than that in backward, and the mean values in two directions were in the range of 3.84 to 4.23. From the comparison of specimens S-1 and S-3 as well as that of S-2

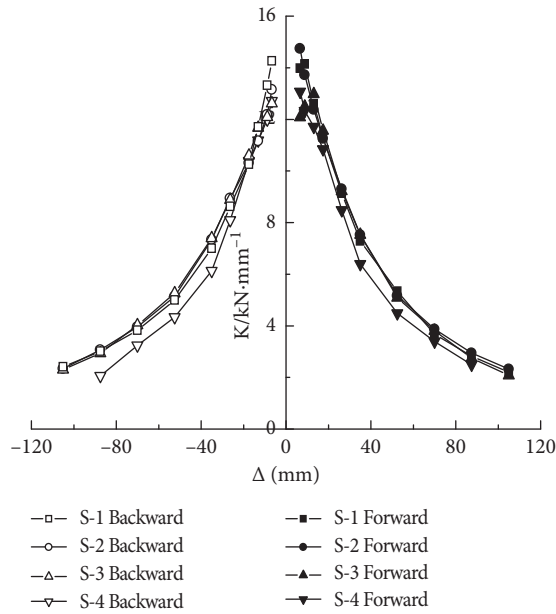


FIGURE 10: Loop rigidity coefficient (K) vs. displacement Δ .

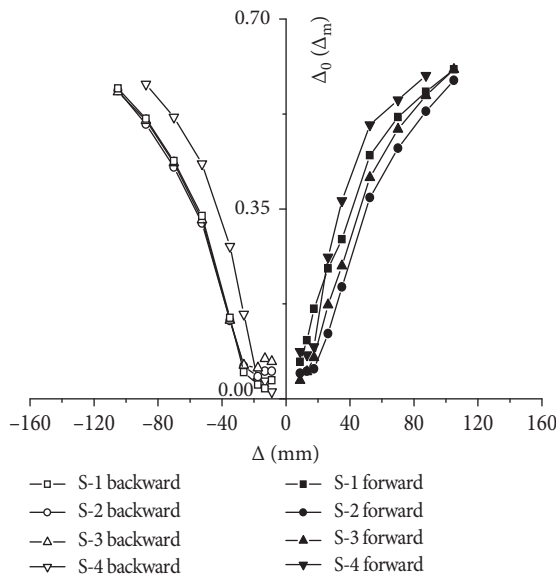


FIGURE 11: Residual deformation ratio Δ_0/Δ_m vs. displacement Δ .

and S-3, the displacement ductility could be reduced by increasing the prestressing levels or the axial compressive ratios. Besides, due to the fact that the damage at beam ends was worse than that in the panel zone and different failure modes were observed compared with prestressed specimens, the displacement ductility for specimen S-4 was not the best.

4.6. Shear Deformations in Panel Zones. Table 5 gives the shear deformation in panel zones for all the specimens, where γ_y and γ_p are the shear deformation at yielding and peak loads, respectively. The following are observed:

- (1) The ratios of shear deformation under peak load to yield load (γ_p/γ_y) were in the range of 3.96~6.05 for specimens S-1, S-2, and S-3, which showed that the shear deformation in panel zones developed sufficiently after yielding, and good shear deformation capacities were observed.
- (2) When the prestressing levels enhanced from 0.39 to 0.50 for specimens S-1 and S-3, where the increasing amplitude was about 28%, the shear deformation at yielding and peak loads reduced by 22% and 43%, respectively; however, when the axial compressive ratios increased to about two times according to specimens S-2 and S-3, the shear deformation at yielding and peak loads reduced by 25% and 51%, respectively, which indicated that the prestressing level played a more dominant role than axial compressive ratios in reducing the shear deformation.
- (3) Compared with prestressed joint specimens, the shear deformations at yielding and peak loads for specimen S-4 were the highest and smallest values, respectively. The reason for this was that the shear deformation mostly concentrated in the panel zone due to the lack of prestressing before yielding, and after that, the plastic hinges at beam ends were fully developed to bending failure; thus, the shear deformation in panel zones had no significant growth.

4.7. Strain Analysis. In order to study the strain variations of I-steels, steel tubes, longitudinal rebars, and stirrups, strains of the measuring points for all specimens were obtained in tests, and relationships of lateral loads and strains were plotted. Since the strain changes were basically the same for prestressing specimens, some strains of typical measuring points were analysed in this paper.

The strain changes of stirrups and steel tube in the panel zone at measuring points 18 and 19 for specimen S-1 are given in Figure 12. As can be seen from Figure 12(a), the stirrups eventually reached tensile yielding, which means that the stirrups were able to bear a portion of shear force in the panel zone. The shear strains of steel tube shown in Figure 12(b) were obtained by the fixed strain rosettes at measuring point 19, and it was observed that the shear strains were in line before yielding, and a certain degree of pinching was found as the lateral loading increased after that.

Figure 13 gives the strains changes of longitudinal rebar and I-steel flange at measuring points 5 and 30 for specimen S-2, which were in the upper side at the left beam end. It can be seen that the longitudinal rebar and I-steel flange reached yielding under sagging and hogging moments, and the plastic hinges formed at beam ends.

Figure 14 gives the strain variations of longitudinal rebar and steel tube at upper column ends, where the measuring points 24 and 26 were located on the left and right of the steel tube and measuring point 25 was in the middle. It can be seen that almost all the measuring points were in the compression condition during the whole loading, and no plastic hinges formed at column ends. In particular, it was observed that the strains of the steel tube were almost

TABLE 4: Displacement ductility factor of specimens.

Specimens	Loading direction	Yielding load P_y (kN)	Yielding displacement Δ_y (mm)	Peak load P_u (kN)	Ultimate displacement Δ_u (mm)	Displacement ductility factor ($\mu = \Delta_u/\Delta_y$)	Mean displacement ductility factors ($\bar{\mu}$)
S-1	Forward	224.1	23.6	255.4	105.0	4.46	4.23
	Backward	-233.8	-26.3	-262.9	-105.0	3.99	
S-2	Forward	235.6	24.7	271.4	104.0	4.21	3.96
	Backward	-239.1	-28.2	-273.2	-104.4	3.71	
S-3	Forward	239.7	25.8	261.1	101.6	3.93	3.79
	Backward	-239.2	-28.7	-273.4	-105.0	3.65	
S-4	Forward	204.8	22.1	233.7	87.5	3.96	3.84
	Backward	-190.6	-22.2	-225.4	-82.6	3.72	

TABLE 5: Shear deformations in panel zones.

Specimens	Shear deformation at yielding load γ_y (rad)	Shear deformation at peak load γ_p (rad)	γ_p/γ_y
S-1	6.8×10^{-3}	3.7×10^{-2}	5.44
S-2	7.1×10^{-3}	4.3×10^{-2}	6.05
S-3	5.3×10^{-3}	2.1×10^{-2}	3.96
S-4	7.3×10^{-3}	1.6×10^{-2}	2.19

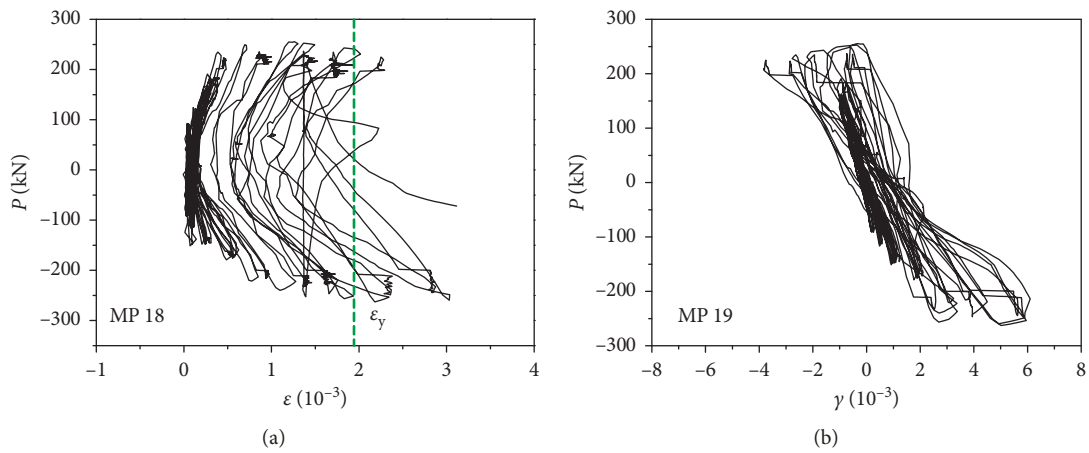


FIGURE 12: Strain changes in the panel zone: (a) strain of stirrups; (b) shear strain of the steel tube.

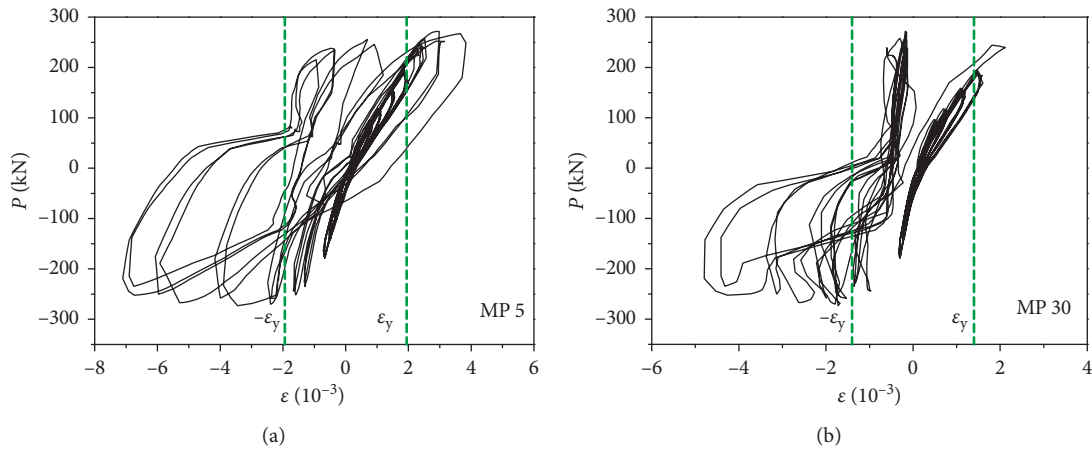


FIGURE 13: Strains at beam end: (a) longitudinal rebar; (b) I-steel flange.

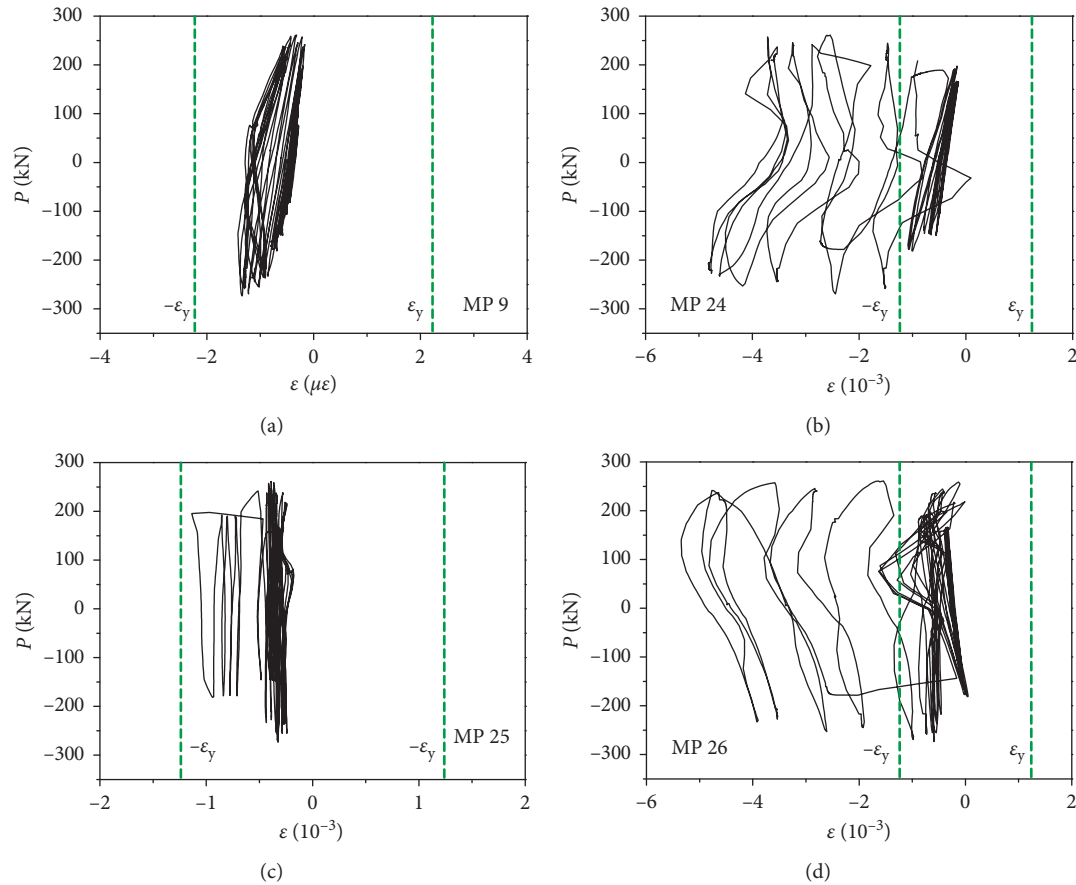


FIGURE 14: Strains of longitudinal rebars and steel tube at the upper column end: (a) longitudinal rebars; (b) left side of the steel tube; (c) middle of the steel tube; (d) right side of the steel tube.

proportional to lateral loads at the initial period of loading, and the strains increase with the increase of lateral load, in which the measuring points 24 and 26 reached yield. The reason for the yielding of the steel tube was that the yield strength of the steel tube was lower than that of longitudinal rebars, and the outer edges of the steel tube were the first to reach the yield strains. The strain variations of longitudinal rebars and steel tube at the lower column end were analogous. Overall, the test results were consistent with the design objective of “strong column and weak beam.”

5. Discussion

Since only experimental studies on hysteretic behaviour under different axial compression ratios and prestressing levels were performed, more investigation should be needed in order to propose the design methods for the innovative prestressed composite frame joints. To achieve this objective, numerical models will be established and verified, and mechanical mechanism and parameter analysis will be conducted in further studies.

6. Conclusions

Tests on three prestressed and one non-prestressed interior joint specimens with concrete-encased CFST columns were

performed under lateral cyclic loading, and the following conclusions were achieved:

- (1) The lateral load-displacement hysteretic curves of all specimens were plump, and it means that joint specimens which were prestressed also showed good ductility and energy dissipation capacity.
- (2) All prestressed joint specimens represented the mixed modes consisting of flexural failure at beam ends and shear failure in panel zones, whilst only flexural failure at beam ends was observed in the non-prestressed joint.
- (3) When the prestressing levels increased by 28%, the shear deformations in panel zones at yielding and peak loads decreased by 22% and 43%, respectively; however, when the axial compressive ratios increased by about two times, the corresponding shear deformations were reduced by 25% and 51%, respectively.
- (4) Enhancing prestressing level could postpone the appearance of first cracks at beam ends and increase the peak loads for prestressed specimens. The axial compression ratio had limited effect on the peak loads, whilst the ductility and energy dissipation capacity could be reduced in some degree as the axial compression ratio increased.

Data Availability

The data used to support the findings of this study are available from the corresponding author upon request.

Conflicts of Interest

The authors declare that they have no conflicts of interest.

Acknowledgments

The authors appreciate the support of National Science Foundation of China (51878589 and 51578478), Six Talent Peaks Project of Jiangsu Province (2017-JZ-038), Science and Technology Planning Project of Yangzhou City (YZ2018068), and the Talent Project of Excellent Young Teacher of Yangzhou University (2016).

References

- [1] L. Fang, B. Zhang, G.-F. Jin, K.-W. Li, and Z.-L. Wang, "Seismic behavior of concrete-encased steel cross-shaped columns," *Journal of Constructional Steel Research*, vol. 109, pp. 24–33, 2015.
- [2] Y. H. Wang, J. G. Nie, and C. S. Cai, "Numerical modeling on concrete structures and steel-concrete composite frame structures," *Composites part B: Engineering*, vol. 51, pp. 58–67, 2013.
- [3] K. Wang, S. F. Yuan, D. F. Cao, and W. Z. Zheng, "Experimental and numerical investigation on frame structure composed of steel reinforced concrete beam and angle-steel concrete column under dynamic loading," *International Journal of Civil Engineering*, vol. 13, no. 2, pp. 137–147, 2015.
- [4] C. G. Fu, Y. Y. Li, X. B. Sun, and J. Xu, "Experimental study on seismic performance of prestressed and non-prestressed steel reinforced concrete frames," *Journal of Building Structure*, vol. 31, no. 8, pp. 15–21, 2010, in Chinese.
- [5] X. Y. Xiong and F. Gao, "Experimental investigation and analysis on large scale prestressed steel reinforced concrete frame," *Journal of Sichuan University (Natural Science Edition)*, vol. 43, no. 6, pp. 1–8, 2011, in Chinese.
- [6] K. Wang, X.-F. Lu, S.-F. Yuan, D.-F. Cao, and Z.-X. Chen, "Analysis on hysteretic behavior of composite frames with concrete-encased CFST columns," *Journal of Constructional Steel Research*, vol. 135, pp. 176–186, 2017.
- [7] K. Wang, S.-F. Yuan, Z.-X. Chen, H.-X. Zhi, G.-L. Shi, and D.-F. Cao, "Experimental study on hysteretic behavior of composite frames with concrete-encased CFST columns," *Journal of Constructional Steel Research*, vol. 123, pp. 110–120, 2016.
- [8] E. Farajpourbonab, "Numerical study of cft columns under axial, eccentric and lateral cyclic loading," *Ingegneria Sismica*, vol. 35, no. 3, pp. 22–42, 2018.
- [9] R. Montuori and V. Piluso, "Analysis and modelling of CFT members: moment curvature analysis," *Thin-Walled Structures*, vol. 86, pp. 157–166, 2015.
- [10] Q. Shi, W. Cai, and B. Wang, "Axial cyclic testing of concrete-filled steel tube columns in diagrid structures," *Advances in Civil Engineering*, vol. 2019, Article ID 4726029, 14 pages, 2019.
- [11] J. Pan, P. Wang, Y. Zheng, Z. Wang, and D. Liu, "An analytical study of square CFT columns in bracing connection subjected to axial loading," *Advances in Civil Engineering*, vol. 2018, Article ID 8618937, 15 pages, 2018.
- [12] B. Xu, F. Wu, and G. Xu, "Mechanism study on the axial compressive performance of short square CFST columns with different stiffeners," *Advances in Civil Engineering*, vol. 2018, Article ID 9109371, 10 pages, 2018.
- [13] L.-H. Han and Y.-F. An, "Performance of concrete-encased CFST stub columns under axial compression," *Journal of Constructional Steel Research*, vol. 93, no. 2, pp. 62–76, 2014.
- [14] Y. F. An and L. H. Han, "Behavior of concrete-encased CFST columns under combined compression and bending," *Journal of Constructional Steel Research*, vol. 101, pp. 314–330, 2014.
- [15] Q. Q. Guo, Y. X. Zhao, Q. Li, and K. Shang, "Experimental study on eccentric compressive property of steel tube-reinforced concrete columns," *Journal of Building Structure*, vol. 34, no. 12, pp. 103–111, 2013, in Chinese.
- [16] L.-H. Han, F.-Y. Liao, Z. Tao, and Z. Hong, "Performance of concrete filled steel tube reinforced concrete columns subjected to cyclic bending," *Journal of Constructional Steel Research*, vol. 65, no. 8–9, pp. 1607–1616, 2009.
- [17] W.-W. Qian, W. Li, L.-H. Han, and X.-L. Zhao, "Analytical behavior of concrete-encased CFST columns under cyclic lateral loading," *Journal of Constructional Steel Research*, vol. 120, pp. 206–220, 2016.
- [18] X. Ji, H. Kang, X. Chen, and J. Qian, "Seismic behavior and strength capacity of steel tube-reinforced concrete composite columns," *Earthquake Engineering & Structural Dynamics*, vol. 43, no. 4, pp. 487–505, 2014.
- [19] X. Ji, M. Zhang, H. Kang, J. Qian, and H. Hu, "Effect of cumulative seismic damage to steel tube-reinforced concrete composite columns," *Earthquakes and Structures*, vol. 7, no. 2, pp. 179–199, 2014.
- [20] J. Liu, F.-X. Ding, X.-M. Liu, Z.-W. Yu, Z. Tan, and J.-W. Huang, "Flexural capacity of steel-concrete composite beams under hogging moment," *Advances in Civil Engineering*, vol. 2019, Article ID 3453274, 13 pages, 2019.
- [21] J. Wang, D. Wu, and W. Z. Zheng, "Experimental research on flexural mechanical behavior of simple prestressed H-steel reinforced concrete beam," *Journal of Harbin Institute of Technology*, vol. 41, no. 6, 2009, in Chinese.
- [22] W. Huang, Z. Lai, B. Chen, and P. Yao, "Experimental behavior and analysis of prestressed concrete-filled steel tube (CFT) truss girders," *Engineering Structures*, vol. 152, pp. 607–618, 2017.
- [23] K. S. Kim, D. H. Lee, S. M. Choi, Y. H. Choi, and S. H. Jung, "Flexural behavior of prestressed composite beams with corrugated web: part I. Development and analysis," *Composites Part B: Engineering*, vol. 42, no. 6, pp. 1603–1616, 2011.
- [24] K. S. Kim and D. H. Lee, "Flexural behavior of prestressed composite beams with corrugated web: part II. Experiment and verification," *Composites Part B: Engineering*, vol. 42, no. 6, pp. 1617–1629, 2011.
- [25] S. C. Choy, Y. L. Wong, and S. L. Chan, "Shear strength of prestressed concrete encased steel beams with bonded tendons," in *Proceedings of the Third International Conference on Advances in Steel Structures (ICASS '02)*, pp. 543–549, Hong Kong, China, December 2002.
- [26] D. Yao, J. Jia, F. Wu, and F. Yu, "Shear performance of prestressed ultra high strength concrete encased steel beams," *Construction and Building Materials*, vol. 52, pp. 194–201, 2014.
- [27] J. Wang, T. S. Zhao, H. Y. Xie, and W. Z. Zheng, "Experimental research on shear carrying capacity of H-steel concrete composite beam with small shear span ratio," *Journal of*

- Harbin Institute of Technology (New Series)*, vol. 17, no. 3, pp. 398–400, 2010.
- [28] Z. Li, Y. Liu, H. Ma, Q. Wang, and Z. Tang, “Seismic performance of full-scale joints composed by concrete-filled steel tube column and reinforced concrete beam with steel plate-stud connections,” *Advances in Civil Engineering*, vol. 2019, Article ID 5476909, 17 pages, 2019.
- [29] J. Qian and Y. Jiang, “Tests on seismic behavior of RC beam to composite steel tube confined concrete column joints,” *Building Structure*, vol. 39, no. 9, pp. 39–42, 2009, in Chinese.
- [30] F. Y. Liao, L. H. Han, and Z. Tao, “Behaviour of composite joints with concrete encased CFST columns under cyclic loading: Experiments,” *Engineering Structure*, vol. 59, pp. 745–764, 2014.
- [31] J. G. Nie, Y. H. Wang, M. X. Tao, and W. Y. Tan, “Experimental study on seismic behavior of laminated steel tube column—concrete beam joint with outer stiffening ring,” *Journal of Building Structure*, vol. 12, no. 7, pp. 88–97, 2012, in Chinese.
- [32] W. W. Qian, W. Li, L. H. Han, and X. L. Zhao, “Behavior of concrete-encased concrete-filled steel tubular column to steel beam joint under cyclic loading,” *China Civil Engineering Journal*, vol. 50, no. 7, pp. 27–38, 2017, in Chinese.
- [33] Z. H. Deng, X. Y. Wang, X. D. Zhang, and Y. S. Fan, “Experimental research on design method for frame joints of concrete-filled steel tubular core columns and prestressed concrete beams,” *Industry Construction*, vol. 36, no. 9, pp. 71–74, 2006, in Chinese.
- [34] R. Montuori, E. Nistri, M. I. Palese, and V. Piluso, “The effect of floor joists on the elastic and inelastic behavior of R.C frames,” *Engineering Structures*, vol. 196, article 109267, 2019.
- [35] R. Montuori, E. Nistri, and V. Piluso, “Modelling of floor joists contribution to the lateral stiffness of RC buildings designed for gravity loads,” *Engineering Structures*, vol. 121, pp. 85–96, 2016.
- [36] L.-H. Han and W. Li, “Seismic performance of CFST column to steel beam joint with RC slab: experiments,” *Journal of Constructional Steel Research*, vol. 66, no. 11, pp. 1374–1386, 2010.
- [37] JGJ3-2010, *Technical Specification for Concrete Structures of Tall Building*, Architecture & Building Press, Beijing, China, 2010, in Chinese.
- [38] GB/T 50152-2012, *Standard for Test Method of Concrete Structures*, Architecture & Building Press, Beijing, China, 2012, in Chinese.
- [39] ANSI/AISC 341-05, *Seismic Provisions for Structural Steel Buildings*, American Institute of Steel Construction, Chicago, IL, USA, 2005.
- [40] R. Park, “Evaluation of ductility of structures and structural assemblages from laboratory testing,” *Bulletin of the New Zealand National Society for Earthquake Engineering*, vol. 22, no. 3, pp. 155–166, 1989.



Hindawi

Submit your manuscripts at
www.hindawi.com

